Available online at www.sciencedirect.com
SCIENCE DIRECT®
International Journal of Heat and Mass Transfer 47 (2004) 3215–3231
International Journal of HEAT and MASS TRANSFER
www.elsevier.com/locate/ijhmt

Centrifugal buoyancy effect on turbulent heat transfer in a rotating two-pass smooth square channel with sharp 180-deg turns

Akira Murata *, Sadanari Mochizuki

Department of Mechanical Systems Engineering, College of Engineering, Tokyo University of Agriculture and Technology, 2-24-16 Nakacho, Koganei, Tokyo 184-8588, Japan

Received 20 November 2003; received in revised form 6 February 2004
Available online 9 April 2004

Abstract

Centrifugal buoyancy effect on heat transfer in a rotating two-pass square channel with 180-deg sharp turns was numerically investigated by using the large eddy simulation. The effect of the aiding/opposing buoyancy contributions was seen in different longitudinal vortex structure near the pressure surface depending on the radial flow direction and in larger buoyancy-induced variation of the heat transfer on the pressure surface than that on the suction surface. As the buoyancy increased, the friction factor dominated by the pressure loss of the sharp turn decreased a little, and the Colburn's j factor stayed almost constant. As a result, the heat transfer efficiency index slightly increased by the buoyancy.

1. Introduction

The effective cooling of a gas turbine rotor blade is essential because higher efficiency of the turbine requires higher inlet gas temperature. Generally, this blade cooling is performed by film cooling at the external surface of the turbine blade and also by internal forced-convection cooling which uses winding flow passages inside the turbine blade. In the internal forced-convection cooling, the real phenomena are very complicated due to external forces: the Coriolis force and the buoyancy force in the centrifugal acceleration field. In addition to these external forces, the disturbances induced by turbulence promoters (ribs) and 180-deg sharp turns further complicate the phenomena [1].

As for the heat transfer in smooth and/or rib-roughened channels with the 180-deg sharp turn, several researchers investigated the detailed spatial variation of the local heat transfer in the stationary condition with various techniques: wall temperature measurement by using hundreds of thermocouples [2,3], naphthalene sublimation technique to measure the local mass transfer, which was transformed into heat transfer by using the analogy between heat and mass transfer [4,5], unsteady wall temperature measurement by using temperature-sensitive liquid crystal [6,7], and wall temperature measurement by using infrared thermography [8]. In these studies, the heat transfer variation induced by the 180-deg sharp turn was captured: the high heat transfer areas were observed in and after the sharp turn. As for the flow field in the stationary condition, Son et al. [9] applied the particle image velocimetry technique to the two-pass channel with the 180-deg sharp turn, and the detailed two-dimensional flow field was measured. For the rotating condition, however, both flow velocity and wall temperature measurements become very difficult because of the following two reasons: high centrifugal force preventing data acquisition system from normal operation in the rotating system and the difficulty in transferring data from the rotating system to the stationary system. Nevertheless, some researchers have

* Corresponding author. Tel.: +81-42-388-7089; fax: +81-42-385-7204.
E-mail address: murata@mmlab.mech.tuat.ac.jp (A. Murata).

0017-9310/$ - see front matter © 2004 Elsevier Ltd. All rights reserved.
doi:10.1016/j.ijheatmasstransfer.2004.02.013

Nomenclature

$A_{\text{total,nodim}}$ dimensionless total heat transfer area of channel
c_p specific heat, J/(kg K)
C_S Smagorinsky constant
C_θ coefficient of linear component in energy equation ($=A_{\text{total,nodim}}/32$)
D hydraulic diameter (= side length of straight pass cross-section), m
f friction factor ($=\Delta p_{\text{total}} D/(2\rho U_m^2 L)$)
F_i external force term
Gr_* Grashof number based on friction temperature ($=\beta T_r \omega^2 R_{m,\text{dim}} \ell^3/\nu^2$)
$Gr_{m,q}$ Grashof number based on wall heat flux ($=\beta \dot{q} \omega^2 R_{m,\text{dim}} D^4/(\nu^2 \lambda)$)
$Gr_{m,\Delta T}$ Grashof number based on temperature difference ($=\beta \Delta T \omega^2 R_{m,\text{dim}} D^3/\nu^2$)
h heat transfer coefficient, W/(m^2 K)
H_0 dimensionless distance between rotation axis and x-axis ($=H_{0,\text{dim}}/\ell$)
$H_{0,\text{dim}}$ distance between rotation axis and x-axis ($z=0$), m
j Colburn's j factor ($=Nu_m/(Re_m Pr^{1/3})$)
k dimensionless turbulent kinetic energy
K_{straight} pressure loss coefficient of straight pass ($=\Delta p_{\text{straight}}/(\frac{1}{2}\rho U_m^2)$)
K_{turn} pressure loss coefficient of sharp turn ($=\Delta p_{\text{turn}}/(\frac{1}{2}\rho U_m^2)$)
ℓ length scale ($=0.5D$), m
L total duct-axial length of two-pass channel ($=22D$), m
Nu Nusselt number ($=hD/\lambda$)
$\Delta p_{\text{straight}}$ pressure loss at straight pass, Pa
Δp_{total} pressure loss between channel inlet and outlet, Pa
Δp_{turn} pressure loss between turn inlet and outlet, Pa
Pr Prandtl number ($=0.71$)
Pr_{SGS} Prandtl number of subgrid-scale model ($=0.5$)
$\dot{q}$ wall heat flux, W/m^2
Q second invariant of deformation tensor
R_m dimensionless mean rotation radius ($=R_{m,\text{dim}}/\ell$)
$R_{m,\text{dim}}$ mean rotation radius, m
Ra_* Rayleigh number ($=Gr_* Pr$)
Re_m Reynolds number based on bulk mean velocity ($=U_m D/\nu$)
Re_* Reynolds number based on friction velocity ($=u_* \ell/\nu$)
Ro_m rotation number based on bulk mean velocity ($=\omega D/U_m$)
Ro_* rotation number based on friction velocity ($=\omega \ell/u_*$)
S_{ij} rate-of-strain tensor
St Stanton number ($=Nu_m/(Re_m Pr)$)
t dimensionless time
ΔT mean temperature difference between wall and fluid ($=(T_w - T_b)_m$), K
T temperature, K
T_{linear} linearly increasing component of temperature, K
T_r friction temperature ($=\dot{q}/(\rho c_p u_*)$), K
u, v, w dimensionless velocities in x, y, z-directions
u_* mean friction velocity calculated from mean pressure gradient in x-direction, m/s
$u_{*\text{mod}}$ mean friction velocity estimated by using bulk mean velocity, m/s
$\bar{u}_m$ dimensionless bulk mean velocity in x-direction calculated at the entrance $\left(=\frac{1}{4}\int_{-1}^{1}\int_{-1}^{1} \bar{u}\,dy\,dz\right)$
U_m bulk mean velocity, m/s
x, y, z dimensionless Cartesian coordinates
$\alpha_{\text{SGS}j}$ subgrid-scale energy flux
β expansion coefficient, 1/K
$\Delta_1, \Delta_2, \Delta_3$ grid spacing in ξ, η, ζ, directions expressed in (x, y, z) coordinates' scale
η_{eff} heat transfer efficiency index ($=(St/St_{\text{smooth,stationary}})/(f/f_{\text{smooth,stationary}})^{1/3}$)
λ thermal conductivity, W/(m K)
ν kinematic viscosity, m^2/s
ν_{SGS} dimensionless subgrid-scale eddy viscosity
ω angular velocity, rad/s
ρ density, kg/m^3
θ dimensionless temperature ($=(T - T_{\text{linear}})/T_r$)
$\tau_{\text{SGS}ij}$ subgrid-scale stress tensor
$\tau_{w,s}$ streamwise component of wall shear stress, Pa
ξ, η, ζ curvilinear coordinates

Subscripts and superscripts

b bulk value
B Blasius
L local value
m duct average or based on bulk mean velocity
w wall
∞ fully developed or ambient
$*$ friction velocity or defined by using u_*
$+$ dimensionless value based on inner scales
$-$ grid resolvable component

performed measurements in the rotating condition by measuring the wall temperature distribution using thermocouples for the smooth [10–12] and rib-roughened [13–15] wall two-pass channels with the 180-deg sharp turn. Liou et al. [16] performed the flow velocity measurement of a rotating two-pass smooth channel with the 180-deg sharp turn by using the laser Doppler anemometer in addition to the detailed heat transfer measurement by using the transient liquid crystal method. However, it is very difficult to perform the experiments in the rotating condition which can identify both the flow structure and its influence on the heat transfer at the same time. Thus, further progress in experimental studies has so far been prevented.

In previous numerical studies of the serpentine flow passage with the 180-deg sharp turn, the Reynolds-averaged Navier–Stokes equation with a turbulence model was adopted: Banhoff et al. [17] used the k–ε two-equation turbulence model or the Reynolds stress equation model with the wall function, and Lin et al. [18] used the low-Reynolds number two-equation turbulence model without the wall function. Although this approach using the Reynolds-averaged turbulence model could reproduce the heat transfer of blade cooling to a certain extent, even the Reynolds stress equation model has empirical constants and functions, and therefore the applicability of the model should carefully be examined. Recent advancement in computers enables us to numerically simulate fluctuating components of turbulent flow by using the large eddy simulation (LES) or the direct numerical simulation (DNS), and the techniques were applied to the smooth straight duct in the stationary [19–21] and rotating [22,23] conditions. Because LES and DNS directly resolve temporal variation of the fluctuating components, the results are more universal, in other words, more free from the empirical modeling than the Reynolds-averaged turbulence models. Although LES also has empirical constants and functions, the modeling of the turbulence is confined to the subgrid-scale turbulence, and therefore the effect of the empirical modeling on the result is ideally less than that in the Reynolds stress equation model. Recently, the authors performed the numerical analyses by using a dynamic subgrid-scale model for a rotating angled-rib-roughened straight duct using a coordinate system fitted to the angled ribs [24,25]. Very recently, the authors further proceeded to numerically investigate the effect of the 180-deg sharp turn on the fluid flow and heat transfer, and the heat transfer variation was reproduced for the two-pass smooth [26] and rib-roughened [27] channels with the 180-deg sharp turn in the stationary and rotating conditions. Although the effect of the buoyancy force in the centrifugal acceleration field is very important considering the highly severe thermal condition with high rotation rate to which the real turbine blades are exposed [25], the buoyancy effect was ignored in our previous studies of the two-pass channel with the 180-deg sharp turn [26,27].

This study examines how the centrifugal buoyancy force affects the heat transfer in the rotating two-pass channel with 180-deg sharp turns. The computations were performed varying the Rayleigh number that represents the intensity of the buoyancy force. The attention was paid to the relation between the main flow and centrifugal buoyancy force directions, because the heat transfer of radially outward and inward flow cases differs due to aiding and opposing buoyancy contributions to the flow.

2. Numerical analysis

Fig. 1 shows the computational domain and coordinate system used in this study. The duct had a square cross-section with a side length of D. The coordinate system was fixed to a rotating channel that had an angular velocity of ω with respect to the axis of rotation parallel to the x-axis. The axial direction of the channel straight pass was chosen in the z-direction; the x- and y-directions were the parallel and perpendicular direction to leading/trailing walls, respectively. The inner and outer walls at the turn A was called the inner and outer walls, respectively. Therefore, it should be noted that "the inner wall" and "the outer wall" of this study came to the outer and inner sides at the turn B, respectively, unless otherwise mentioned. The present procedure of the numerical analysis was the same as our recent studies [26,27]. After applying a filtering operation to the incompressible Navier–Stokes equation with a filter width equal to the grid spacing [21], the dimensionless governing equations scaled by a length scale, $\ell\,(=0.5D)$, and mean friction velocity, u_*, became a set of dimensionless governing equations with respect to grid resolvable components indicated by overbars as $(\bar{u}, \bar{v}, \bar{w})$ under the assumption of constant fluid properties. In order to simulate a fully developed situation, the pressure and temperature fields were decomposed into the steady and x-directionally linear component and the remaining component [28]. By this decomposition, the latter component of the pressure and temperature fields can be treated using a periodic boundary condition in the x-direction.

The temperature was made dimensionless by using a linearly increasing component of temperature, T_{linear}, and a friction temperature, T_{r}, as $\theta = (T - T_{\text{linear}})/T_{\text{r}}$. Accordingly, the dimensionless energy equation was derived for the grid resolvable component, $\bar{\theta}$. The governing equations in the Cartesian coordinates (x, y, z) were transformed into generalized curvilinear coordinates (ξ, η, ζ). At the middle of the first straight pass, the ξ-, η-, and ζ-directions coincided with the x-, y-, and

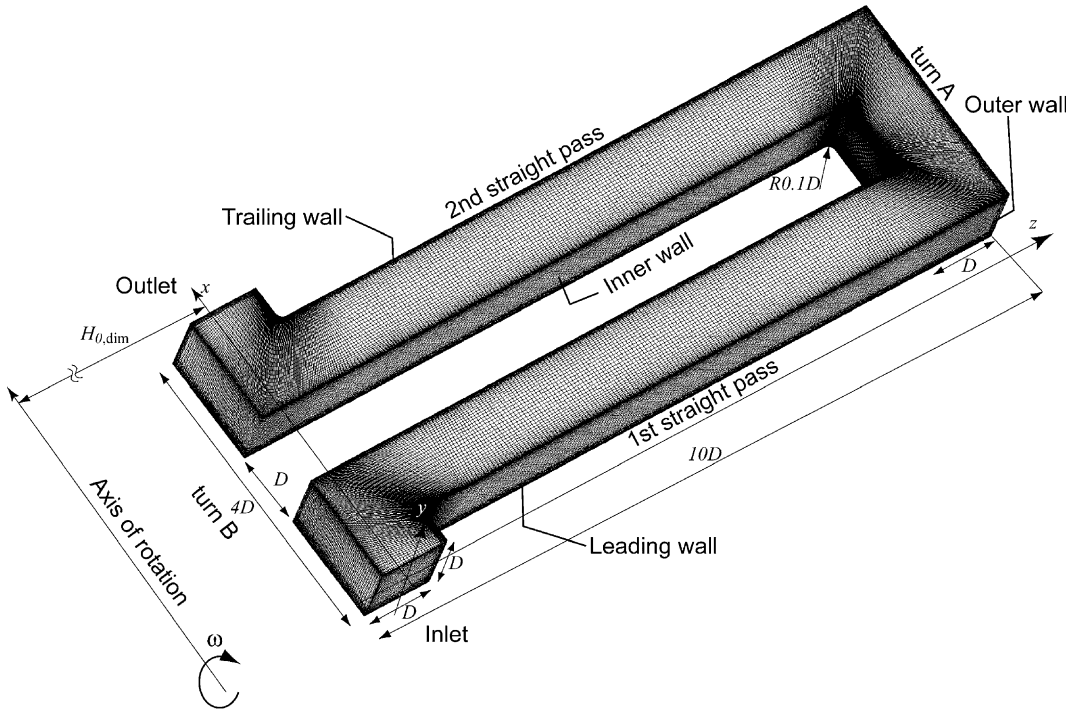

Fig. 1. Schematic of a rotating two-pass smooth square channel with sharp 180-deg turns.

z-directions, respectively. The governing equations in the curvilinear coordinate system were expressed as follows [29]:

$$\frac{1}{J}\frac{\partial J\overline{U}^j}{\partial \xi^j} = 0, \tag{1}$$

$$\frac{\partial \bar{u}_i}{\partial t} = -\overline{U}^j \frac{\partial \bar{u}_i}{\partial \xi^j} - \frac{\partial \xi^j}{\partial x_i}\frac{\partial \bar{p}}{\partial \xi^j} + \frac{1}{Re_*}\frac{\partial \xi^j}{\partial x_\ell}\frac{\partial}{\partial \xi^j}\left(\frac{\partial \xi^k}{\partial x_\ell}\frac{\partial \bar{u}_i}{\partial \xi^k}\right) + \frac{\partial \xi^k}{\partial x_j}\frac{\partial \tau_{\mathrm{SGS}ij}}{\partial \xi^k} + F_i, \tag{2}$$

$$\frac{\partial \bar{\theta}}{\partial t} = -\overline{U}^j \frac{\partial \bar{\theta}}{\partial \xi^j} - C_\theta \frac{\bar{u}}{\bar{u}_\mathrm{m}} + \frac{1}{Re_* Pr}\frac{\partial \xi^j}{\partial x_\ell}\frac{\partial}{\partial \xi^j}\left(\frac{\partial \xi^k}{\partial x_\ell}\frac{\partial \bar{\theta}}{\partial \xi^k}\right) + \frac{\partial \xi^k}{\partial x_j}\frac{\partial \alpha_{\mathrm{SGS}j}}{\partial \xi^k}, \tag{3}$$

where $\overline{U}^j$ was a contravariant component of velocity, and the following expressions were assumed: $J = \partial(x,y,z)/\partial(\xi,\eta,\zeta)$, $(x_1,x_2,x_3) = (x,y,z)$, and $(\xi^1,\xi^2,\xi^3) = (\xi,\eta,\zeta)$. An external force term, F_i, in the momentum equations (Eq. (2)) had the Coriolis force, the centrifugal buoyancy force with the Boussinesq approximation, and the mean pressure gradient term with a value of two as shown in the following equation:

$$F_i = \begin{pmatrix} 2 \\ 2Ro_*\bar{w} - \dfrac{Gr_*}{Re_*^2}\dfrac{(\bar{\theta}-\bar{\theta}_\infty)y}{R_\mathrm{m}} \\ -2Ro_*\bar{v} - \dfrac{Gr_*}{Re_*^2}\dfrac{(\bar{\theta}-\bar{\theta}_\infty)}{R_\mathrm{m}}(H_0+z) \end{pmatrix}. \tag{4}$$

Because the dimensionless mean rotation radius, R_m, is much larger than y and z in the real gas turbines, the following approximation can be used: $y/R_\mathrm{m} \fallingdotseq 0$ and $(H_0+z)/R_\mathrm{m} \fallingdotseq 1$. In the dimensionless reference temperature of $\theta_\infty = (T_\infty - T_{\mathrm{linear}})/T_\mathrm{r}$, T_{linear} changes linearly in the x-direction, and therefore $\bar{\theta}_\infty$ also changes linearly in the x-direction. From the energy balance, the following equation holds:

$$\bar{\theta}_\infty = -C_\theta \frac{x}{\bar{u}_\mathrm{m}}. \tag{5}$$

Consequently Eq. (4) was approximated as follows:

$$F_i = \begin{pmatrix} 2 \\ 2Ro_*\bar{w} \\ -2Ro_*\bar{v} - \dfrac{Gr_*}{Re_*^2}(\bar{\theta}-\bar{\theta}_\infty) \end{pmatrix}. \tag{6}$$

In this study, the mean friction velocity, u_*, was calculated from the force balance between the mean pressure gradient in the x-direction and the wall shear stress as follows:

$$\rho u_*^2 = \frac{\ell}{2}\left|\frac{\mathrm{d}p}{\mathrm{d}x}\right|_{m,\mathrm{dim}}. \tag{7}$$

Here, the mean pressure gradient with the subscript, "dim", means the value with dimension, and it drives the flow in the x-direction. By non-dimensionalizing Eq. (7), the dimensionless mean pressure gradient value of 2 came out. Because the mean pressure gradient which drove the flow in the x-direction was set to be constant in this study, the flow rate varied depending on the flow condition (the rotation number and the Rayleigh number); therefore, the flow rate was not known a priori, and it was calculated from the resultant computed flow field after the fully developed condition was attained. In this study, the fully developed condition was judged by the statistical steadiness.

Subgrid-scale components of stress, $\tau_{\mathrm{SGS}ij}$, and energy flux, $\alpha_{\mathrm{SGS}j}$, were expressed as follows:

$$\tau_{\mathrm{SGS}ij} = 2\nu_{\mathrm{SGS}}\overline{S}_{ij}, \tag{8}$$

$$\alpha_{\mathrm{SGS}j} = \frac{\nu_{\mathrm{SGS}}}{Pr_{\mathrm{SGS}}}\frac{\partial\xi^k}{\partial x_j}\frac{\partial\bar{\theta}}{\partial\xi^k}, \tag{9}$$

where

$$\overline{S}_{ij} = \frac{1}{2}\left(\frac{\partial\xi^k}{\partial x_j}\frac{\partial\bar{u}_i}{\partial\xi^k} + \frac{\partial\xi^k}{\partial x_i}\frac{\partial\bar{u}_j}{\partial\xi^k}\right), \tag{10}$$

$$\nu_{\mathrm{SGS}} = C_{\mathrm{S}}^2(\Delta_1\Delta_2\Delta_3)^{2/3}\sqrt{2\overline{S}_{ij}\overline{S}_{ij}}. \tag{11}$$

Because the flow field of this study has no homogeneous direction, we adopted the Lagrangian dynamic subgrid-scale model of Meneveau et al. [30] which averages the value of C_{S} along a path-line for a certain distance. As for the coefficient of the Lagrangian averaging time scale, the same value of 1.5 as that in [30] was used. The turbulent Prandtl number for the subgrid-scale component, Pr_{SGS}, was set to 0.5 [31]. These values were mainly tested for the two-dimensional channel turbulence, and therefore there is room for further optimization of them to the present complicated flow passage. However, it should be noted that the results in [30] showed acceptably small sensitivity to the coefficient of the Lagrangian averaging time scale, and the value of Pr_{SGS} also showed small sensitivity to the flow types and grid resolution in [31]. The width of the test filter was double the grid spacing.

Discretization was performed by a finite difference method using the collocated grid system [29]. The spatial and temporal discretization schemes were similar to those of Gavrilakis [20]: the second order central differencing method and the Crank–Nicolson method for the viscous term, and the second order differencing method satisfying the conservative property [29] and the second order Adams–Bashforth method for the convective term. The external force term was also treated by the second order Adams–Bashforth method. The pressure field was treated following the MAC method [32]. At the wall boundary, no-slip and constant heat flux conditions were imposed. At the inlet and outlet boundaries, the periodic boundary condition [28] was imposed in order to obtain a fully developed flow. The boundary conditions of the intermediate velocities and pressure were set following the procedure of [33,34].

The local Nusselt number, Nu_{L}, was calculated from the wall temperature as follows:

$$Nu_{\mathrm{L}} = \frac{2Re_*Pr}{\bar{\theta}_{\mathrm{w}} - \bar{\theta}_{\mathrm{b}}}. \tag{12}$$

The averaged Nusselt number was calculated by using the integrally averaged temperature difference for the area in question.

As explained above, the bulk mean Reynolds number, Re_{m}, varied depending on the rotation number, Ro_*, and the Rayleigh number, Ra_*. In order to exclude the effects of Re_{m} on the heat transfer, the value of Re_* $(= u_*\ell/\nu)$ was varied depending on Ro_* $(= \omega\ell/u_*)$ so as to keep the values of Re_{m} constant. The adjustment of Re_* due to Ra_* was not performed, because the effect of Ra_* on the flow rate was smaller than that of Ro_*. The resultant combinations of (Re_*, Ro_*) were (1000, 1) and (1500, 2), and, for each Ro_* case, the Rayleigh number, Ra_*, was varied among 0 to 2×10^4. The conversion of the dimensionless numbers of this study (Re_*, Ro_*, Ra_*) defined by the mean friction velocity, the friction temperature, and the length scale of $0.5D$ into those of (Re_{m}, Ro_{m}, $Gr_{\mathrm{m},q}$) defined by the bulk mean velocity, the wall heat flux, and the hydraulic diameter, D, was summarized in Table 1. As you can see in Table 1, Re_{m} values were around 4000, and the computable Re_{m} was limited by the fact that the higher Reynolds number case requires the higher grid resolution. As a try, the higher Re_{m} case of $Re_{\mathrm{m}} \fallingdotseq 10^4$ was also performed as $(Re_*, Ro_*) = (3500, 2)$ by using the highest grid resolution possible with the present computational resource. For this case, Ra_* was extended up to 3×10^4.

In correlating the experimental results, the effect of the buoyancy is often expressed by using the Grashof number, $Gr_{\mathrm{m},q}$, which is defined with the wall heat flux. The following relation holds due to the definition of $Gr_{\mathrm{m},q}$:

$$Gr_{\mathrm{m},q} = 16Re_*PrGr_* = 16Re_*Ra_*. \tag{13}$$

In the real aircraft gas turbine engines, the central region of the operating range is in the order of $Re_{\mathrm{m}} \sim 10^4$, $Ro_{\mathrm{m}} \sim 10^{-1}$, and $Gr_{\mathrm{m},\Delta T}/Re_{\mathrm{m}}^2 \sim 10^{-1}$ [11]. From the definition of Grashof numbers, the following relation holds between $Gr_{\mathrm{m},q}$ and $Gr_{\mathrm{m},\Delta T}$:

$$Gr_{\mathrm{m},q} = Nu_{\mathrm{m}}Gr_{\mathrm{m},\Delta T}. \tag{14}$$

Table 1
Dimensionless number range of this study and the duct averaged values of f and Nu_m

Re_*	Ro_*	Ra_*	Re_m	Ro_m	$Gr_{m,q}$	$\frac{Gr_{m,q}}{Re_m^2}$	$\frac{Gr_{m,\Delta T}}{Re_m^2}$	f/f_B	Nu_m/Nu_∞ $(=f/f_\infty)$
1000	1	0	4028 (4150)	0.99 (0.96)	0	0	0	9.04 (8.58)	2.39 (2.37)
		5×10^3	4199	0.95	8.0×10^7	4.54	0.13	8.41	2.40
		1×10^4	4563	0.88	1.6×10^8	7.68	0.21	7.27	2.38
		2×10^4	5059	0.79	3.2×10^8	12.50	0.31	6.07	2.37
1500	2	0	3926 (3921)	3.06 (3.06)	0	0	0	21.28 (21.33)	2.77 (2.81)
		5×10^3	4251	2.82	1.2×10^8	6.64	0.17	18.51	2.70
		1×10^4	4386	2.74	2.4×10^8	12.48	0.30	17.53	2.75
3500	2	0	9416	2.97	0	0	0	25.07	2.53
		1×10^4	9545	2.93	5.6×10^8	6.15	0.09	24.47	2.48
		3×10^4	9851	2.84	1.7×10^9	17.52	0.24	23.18	2.55

The values in the parentheses are for higher grid resolution of $71\times71\times761$ with reduced sample size of 30,000 steps. The data for $Ra_* = 0$ of $Re_* = 1000$ and 1500 are from Murata and Mochizuki [26].

Note that as compared to the real situation the values of this study are smaller for Re_m because of the limited grid resolution. The buoyancy parameter [11], $Gr_{m,\Delta T}/Re_m^2$, of this study is in the same order of the real situation (see Table 1).

As shown in Fig. 1, the structured grid system was generated by using Gridgen Ver.14 (Pointwise Inc.). The grids in the physical domain were contracted to the walls and the corners. For $Re_* = 1000$ and $Ro_* = 1$, the grid number was $47\times47\times761$ in ξ,η,ζ directions, and this grid configuration gave a grid spacing of $\Delta_1^+ = 0.16$–18.9, $\Delta_2^+ = 0.16$–13.8, and $\Delta_3^+ = 1.7$–18.0 for $Ra_* = 1\times10^4$. Here, the inner length scale of $\nu/u_{*\mathrm{mod}}$ was used, because the friction velocity, u_*, defined in Eq. (7) overestimated the value. In Eq. (7), the streamwise direction was assumed to be in the x-direction, and therefore it cannot account for the longer total flow distance caused by the change of the streamwise direction in the two-pass channel. In order to estimate appropriate inner length and time scales, the friction velocity, $u_{*\mathrm{mod}}$, was calculated by using the resultant flow rate for each condition and the Blasius equation. For $Re_* = 1500$ and $Ro_* = 2$, higher grid resolution of $47\times47\times1207$ in the ζ-direction (grid number was doubled only in the turn section) was adopted because slight oscillation of the flow field was observed in the $47\times47\times761$ grid results. The effect of the grid spacing on the computed result was checked by increasing the grid number to $71\times71\times761$ for several cases, and no major difference was observed as shown in Table 1. The time step interval was $\Delta t = 1.0\times10^{-4}$, which can be expressed as $\Delta t^+ = 0.016$ ($Re_* = 1000$) when made dimensionless by an inner time scale, $\nu/u_{*\mathrm{mod}}^2$. For $Re_* = 3500$ and $Ro_* = 2$, the grid number of $71\times71\times1207$ was used, and this gave $\Delta_1^+ = 0.30$–23.4, $\Delta_2^+ = 0.31$–17.2, and $\Delta_3^+ = 3.2$–24.6. The dimensionless time step interval was $\Delta t^+ = 0.031$ ($Re_* = 3500$). Due to the highest computational load, the grid independency test could not be performed for the case of $Re_* = 3500$. Although the values of Δ_1^+, Δ_2^+, Δ_3^+ and Δt^+ for $Re_* = 3500$ were comparable to those of $Re_* = 1000$ and 1500, the results of $Re_* = 3500$ showed a little change depending on the statistical samples, and it may be due to the sample size shortage. It should be noted that the qualitative reproducibility of the results of $Re_* = 3500$ was confirmed by comparing different statistical samples for the same flow condition, and the conclusions of this study were not changed.

In order to deal with the very high computational load of this study, the computational domain was decomposed into 64 sub-domains in the duct-axial (ζ) direction, and the parallel computing technique was applied. Each sub-domain's computation was performed on a different CPU on HITACHI SR8000 (Information Technology Center, The University of Tokyo). When the algebraic equation for each variable was solved by

using the SOR method, the values at the sub-domain boundaries were transferred to the neighboring sub-domains by using MPI functions in each iteration step.

The computation was started using the result of the similar condition as an initial condition. At first, the calculations were carried out till the statistically steady flow condition was attained. After that, additional 90,000 steps ($t = 9$ or $t^+ = 1440$ for $Re_* = 1000$) were performed for computing the statistical values. This total time step was adopted as the sample size large enough to give the steady statistical values after some preliminary computations changing the sample size.

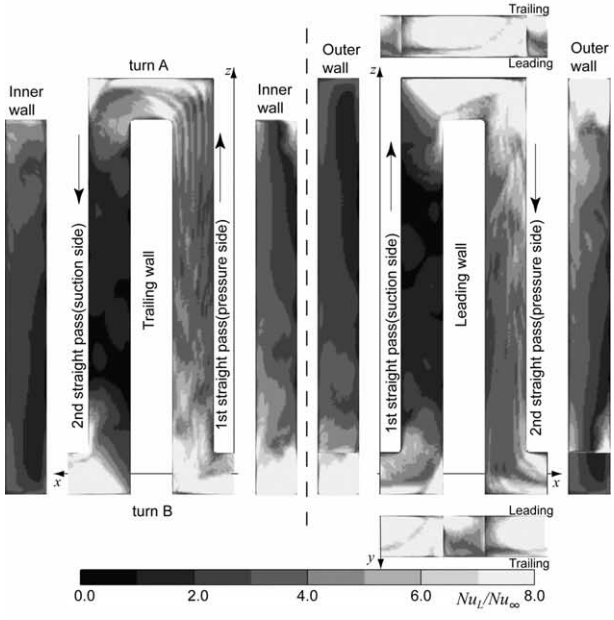

(a) Nusselt number

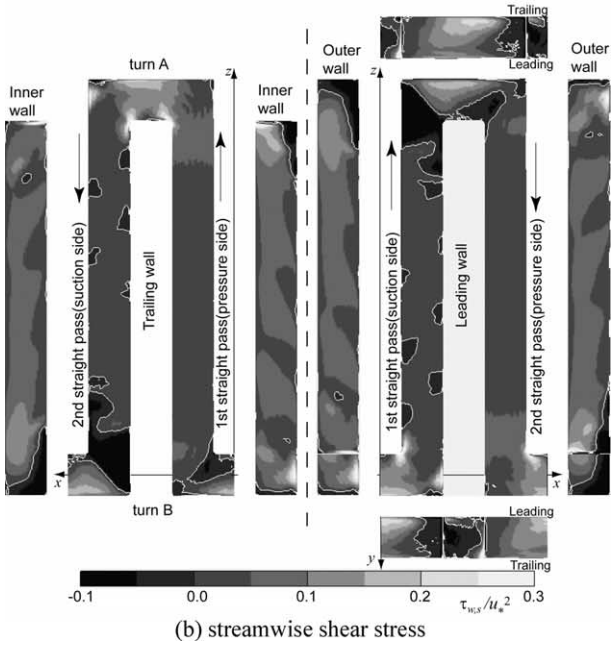

(b) streamwise shear stress

Fig. 2. Time-averaged profiles of Nusselt number and streamwise component of wall shear stress ($Re_* = 1500$, $Re_m = 3926$, $Ro_* = 2$, $Ro_m = 3.06$, and $Ra_* = 0$).

This 90,000 step computation needed about 10.1×64 CPU hours. For the case of $Re_* = 3500$, the sample size was reduced to 80,000 steps that needed about 26.8×64 CPU hours, and however as mentioned above this reduced sample size seemed not to be large enough to give the same level of statistical steadiness as that of $Re_* = 1000$ and 1500.

3. Results and discussion

At first, the verification of the present numerical procedure is explained. In our previous studies of smooth [26] and rib-roughened [27] two-pass channels, the numerical results were compared with the experimental results of the stationary condition in the local

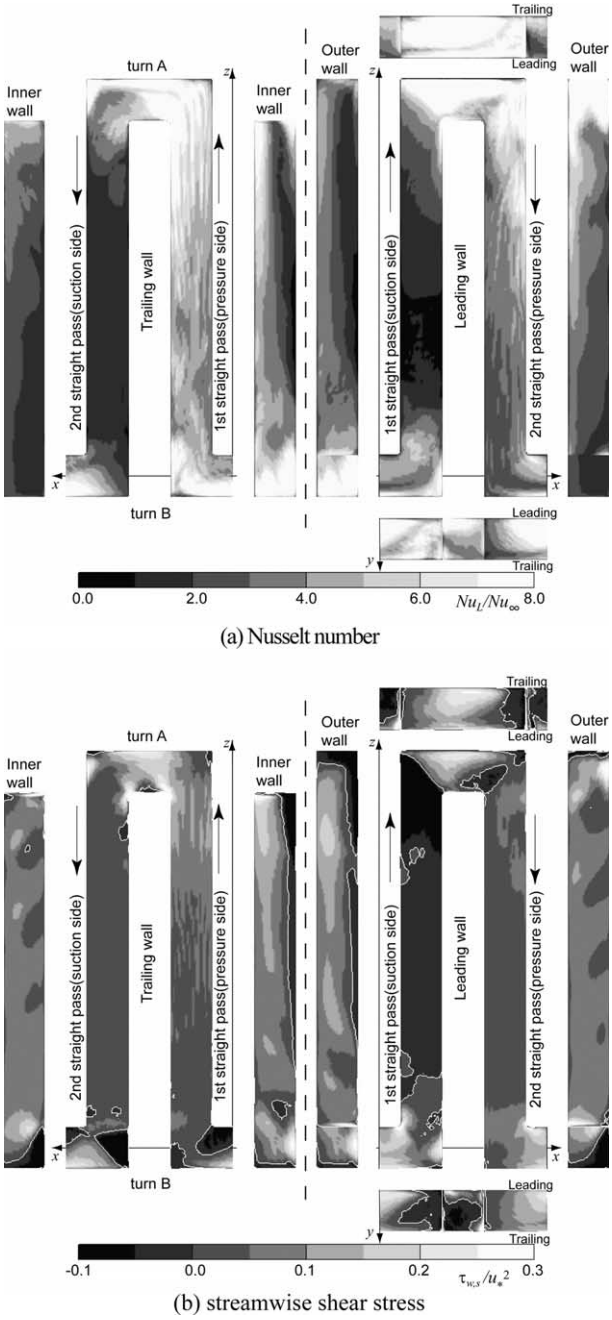

Fig. 3. Time-averaged profiles of Nusselt number and streamwise component of wall shear stress ($Re_* = 1500$, $Re_m = 4386$, $Ro_* = 2$, $Ro_m = 2.74$, and $Ra_* = 1\times10^4$).

and transversely averaged Nusselt numbers and also in the channel averaged f and j factors. The agreement between the numerical and experimental results was good, and the present numerical procedure was able to reproduce the heat transfer enhancement in and after the sharp turn and the quick development of the saw-toothed-profile heat transfer augmentation due to the periodically installed ribs in the straight pass [26,27].

Figs. 2 and 3 show the local Nusselt number (a) and the streamwise component of the wall shear stress (b) on all four walls by viewing the flow channel from six different directions for $Re_* = 1500$ and $Ro_* = 2$. Fig. 2 is the result without the buoyancy force ($Ra_* = 0$), and Fig. 3 is that with the buoyancy force ($Ra_* = 1 \times 10^4$). It should be noted that the lower part of "outer wall" in the figure shows the inner wall values because it is visible through the inlet and outlet of the channel. The Nusselt number of this study was normalized using the following empirical correlation for a fully developed pipe flow [35]:

$$Nu_\infty = 0.022 Re_m^{0.8} Pr^{0.5}. \quad (15)$$

In (b) zero shear stress areas are indicated by a white line. In the calculation of the streamwise component of the wall share stress, the streamwise direction was approximated by the ζ-direction. In this study, the trailing and leading walls of the first straight pass correspond to the pressure and suction surfaces, respectively, and opposite relation holds in the second straight pass. The pressure and suction surfaces are defined with respect to the Coriolis induced secondary flow, which impinges onto the pressure surface. The following differences are caused by introducing the buoyancy force. The Nusselt numbers on the trailing wall in the turn A (especially the upstream half) and the downstream part of the first straight pass are increased, and the streamwise shear stress is also increased in the same area. The reverse flow region in front of the turn A on the leading wall is extended, and it covers almost all the leading wall of the first straight pass; on the other hand, that in front of the turn B on the trailing wall reduces its area.

Figs. 5 and 6 show the isocontours of the time-averaged normal velocity component to the cross-section, $\bar{u}$ or $\bar{w}$, and temperature, $\bar{\theta}$, respectively, for $Re_* = 1500$ and $Ro_* = 2$. (a) and (b) are for $Ra_* = 0$ and 1×10^4, respectively. In the figures, the values at nine different duct-axial locations are shown (see Fig. 4): from top to bottom $x = 4$, $z = 16.9$, 15, 13, 9, 5, 3, 1.1, and $x = 8$ (note that $z = 17$, 9, and 1 correspond to the tip of the inner wall of the turn A, the middle of the straight pass, and the tip of the inner wall of the turn B, respectively, and x and z are normalized by using $\ell = 0.5D$).

For this high rotation speed of $Ro_* = 2$, in the downstream part of the straight pass, the profile of $\bar{w}$ in Fig. 5(a) becomes uniform in the x-direction. This phenomenon is called the Taylor–Proudman effect [36] due to the balance between the pressure gradient and the Coriolis force which does not have a component in the x-direction. Because of the Coriolis induced secondary flow, the fluid temperature on the trailing (pressure) side of the first straight pass becomes lower than that on the leading (suction) side as seen by the low-temperature-peak shift to the pressure side in Fig. 6(a); therefore, on the pressure and suction surfaces of the first straight pass (radially outward flow), the buoyancy works in the aiding and opposing directions to the main flow, respectively (see Fig. 7(a)). On the other hand, in the second straight pass (radially inward flow), the situation is reversed to the first straight pass: on the pressure and suction surfaces of the second straight pass, the buoyancy works in the opposing and aiding directions to the main flow, respectively(see Fig. 7(b)). In this way, when the buoyancy works, the radial flow direction becomes an important parameter which controls the flow and heat transfer.

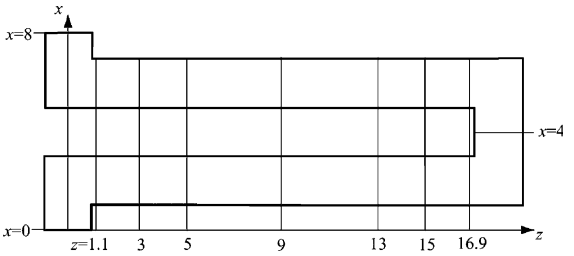

Fig. 4. Locations of planes normal to duct-axis.

When Fig. 5(a) and (b) are compared, the flow in and after the turn are not much affected by the buoyancy. In Fig. 5(b), the buoyancy effect is observed in the extended reversed flow region that is clearly seen on the suction side in the first straight pass ($1 < x < 3$) for $z = 5$–15. The flat profile at $z = 3$ in the second straight pass ($5 < x < 7$) is explained as follows: the reverse flow seen near the suction surface $z = 3$ in Fig. 5(a) disappears due to the aiding contribution of the buoyancy, and, on the other hand, the high streamwise velocity near the pressure surface is decelerated by the opposing contribution of the buoyancy. As shown in Fig. 6, the appearance and disappearance of the reversed flow region drastically change the temperature profiles (see for example $z = 13$ for $1 < x < 3$ and $z = 3$ for $5 < x < 7$).

Fig. 8 shows the turbulent kinetic energy, k, calculated from the grid resolvable components at the same locations as Figs. 5 and 6. In Fig. 8, out-of-range high values are shown by solid black area, and note that the range is doubled for $x = 4$, $z = 16.9$, 1.1, and $x = 8$ because of the high values in and around the turn. The heat transfer enhancement caused by the buoyancy introduction on the pressure surface in the first straight pass (radially outward flow) is usually explained by the

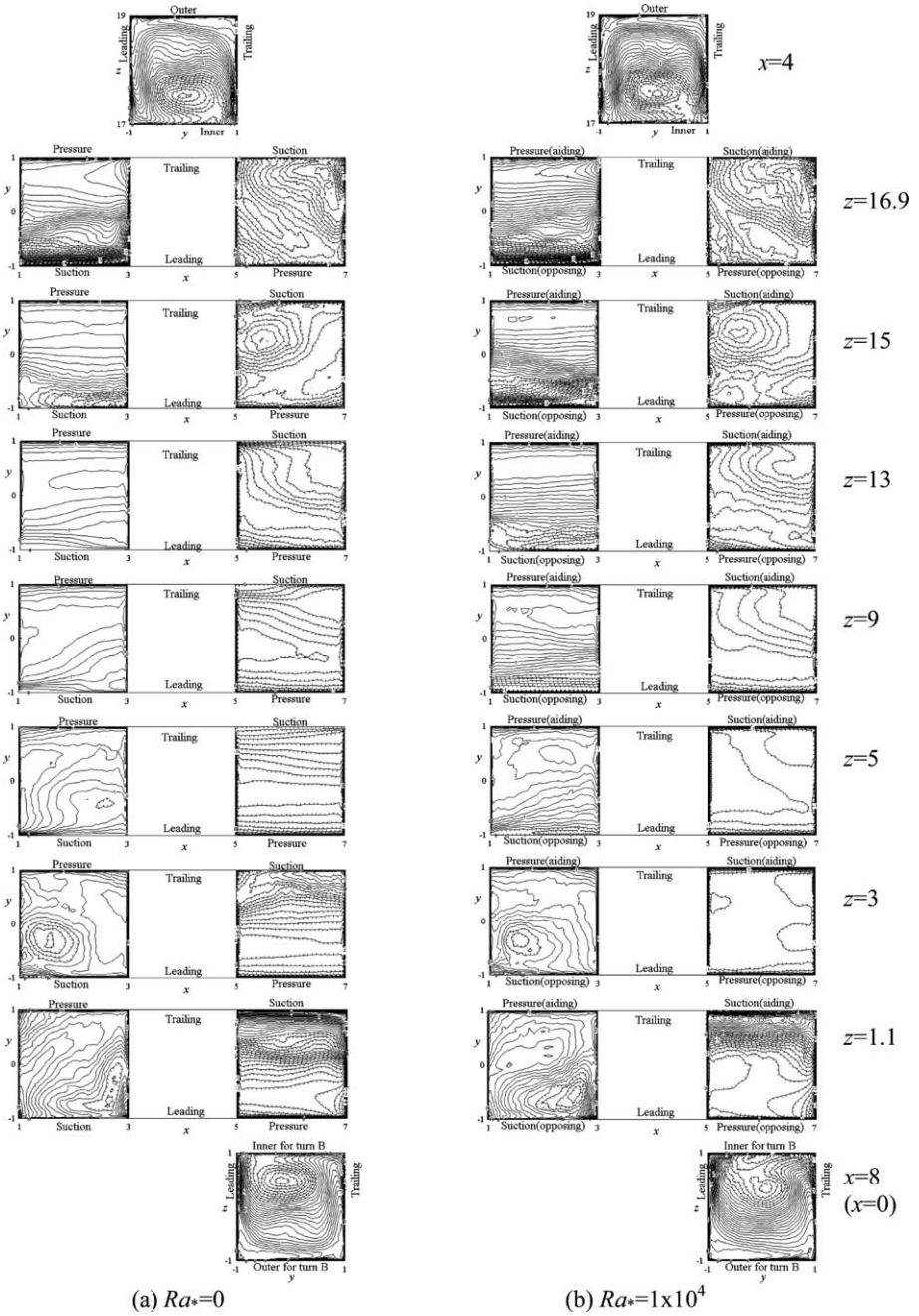

Fig. 5. Buoyancy effect on time-averaged plane-normal velocity component in planes normal to duct-axis for $Re_* = 1500$ and $Ro_* = 2$ (from top to bottom, $x = 4$, $z = 16.9$, 15, 13, 9, 5, 3, 1.1, and $x = 8$. Isocontour lines are drawn by every 0.2).

turbulence production due to the increased shear stress by the buoyancy [11]. As seen in Fig. 8, k is slightly increased in the very vicinity of the trailing (pressure) wall in the first straight pass for $z = 9$–16.9. However, the most discernible change due to the buoyancy introduction is seen in the increased k values in and around the turn, which does not necessarily result in the heat transfer enhancement: for example, in Fig. 8 at $x = 4$ near the inner wall and $z = 1.1$ near trailing (suction) wall in the second straight pass ($5 < x < 7$), the k values are increased very much by the buoyancy, which does not correspond to the heat transfer enhancement that

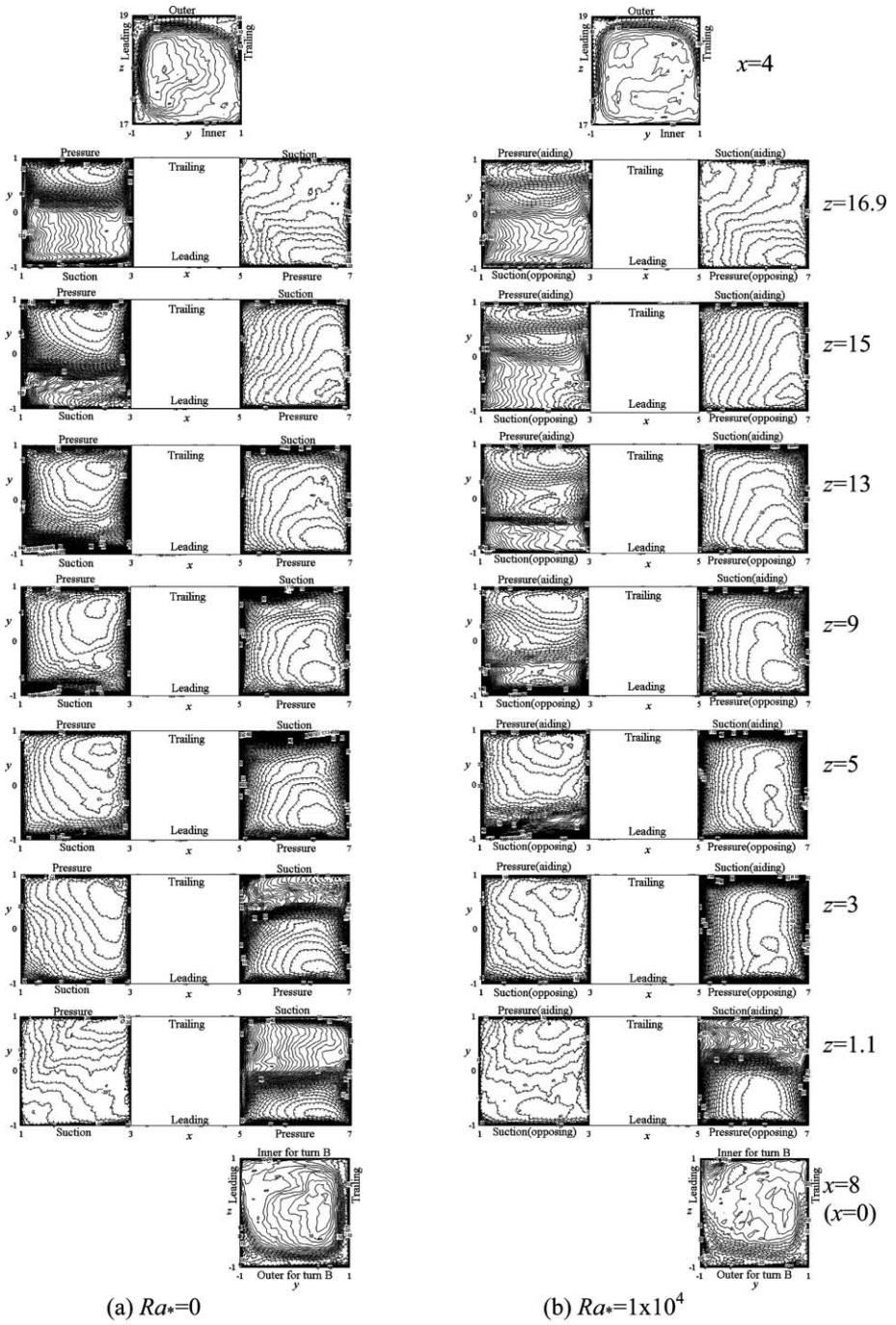

Fig. 6. Buoyancy effect on time-averaged temperature in planes normal to duct-axis for $Re_* = 1500$ and $Ro_* = 2$ (from top to bottom, $x = 4$, $z = 16.9$, 15, 13, 9, 5, 3, 1.1, and $x = 8$. Isocontour lines are drawn by every 2).

much in Fig. 3 as compared to Fig. 2. The intensified shear stress due to the buoyancy introduction results in the larger production of k, and k is increased. However, the heat transfer is strongly affected by the temperature field, and therefore the increased turbulence does not necessarily cause the heat transfer enhancement.

In order to view the flow structure of the whole two-pass channel, the isosurface (surface with the same

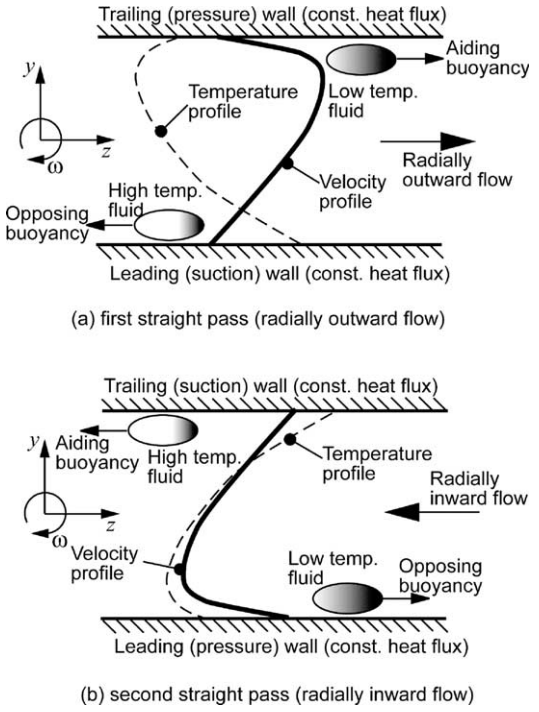

Fig. 7. Explanation of aiding and opposing buoyancy contributions in first (radially outward flow) and second (radially inward flow) straight passes.

value) of the second invariant, Q, of the deformation tensor, $\partial u_i/\partial x_j$, [37] is shown in Fig. 9. The value of Q is calculated by Eq. (16) for incompressible fluids, and it is often used to identify vortices because the positive value of Q means that the vorticity exceeds the strain.

$$\begin{aligned} Q &= \frac{1}{2}\left[\left(\frac{\partial u_i}{\partial x_i}\right)^2 - \left(\frac{\partial u_i}{\partial x_j}\right)\left(\frac{\partial u_j}{\partial x_i}\right)\right] \\ &= -\frac{1}{2}\left(\frac{\partial u_i}{\partial x_j}\right)\left(\frac{\partial u_j}{\partial x_i}\right) \\ &= \frac{1}{2}\left\{\left[\frac{1}{2}\left(\frac{\partial u_i}{\partial x_j} - \frac{\partial u_j}{\partial x_i}\right)\right]^2 - \left[\frac{1}{2}\left(\frac{\partial u_i}{\partial x_j} + \frac{\partial u_j}{\partial x_i}\right)\right]^2\right\}. \end{aligned} \tag{16}$$

As seen in Fig. 9, in and around the turn the strong vortices are produced. The effect of the buoyancy is seen in the different vortex structure near the pressure surfaces in the first and second straight passes: in the first straight pass, the longitudinal vortex structure is maintained by the aiding contribution of the buoyancy, and in the second straight pass the longitudinal vortex structure is weakened and becomes discrete in the streamwise direction due to the opposing contribution of the buoyancy. In front of the turn A, the longitudinal vortex structure near the pressure surface of the first straight pass is somehow very persistent in space, and it is also observed as streaks in the time-averaged fields of Fig. 3.

Fig. 10 shows the duct-axial variation of the area-averaged Nusselt number, Nu_{area}. In order to show the approximate tendency, the area average was taken with the pitch of D (straight pass) or $0.5D$ (turn) in the duct-axial direction for each wall in addition to the transverse average. The thin, middle, and thick line widths correspond to $Ra_* = 0$, 5×10^3, and 1×10^4, respectively. As seen in Fig. 10(a), the outer wall gives the two peaks in the turn, and the buoyancy makes the two peaks lower in the turn B ("inner" in the figure), although it does not affect the values in the turn A. As experimentally observed [11], in Fig. 10(b) the buoyancy enhances the heat transfer on the trailing (pressure) wall in the first straight pass (radially outward flow) strongly; on the other hand, the buoyancy effect is small in the second straight pass (radially inward flow).

In order to examine the buoyancy effect in the developed region, the area-averaged Nusselt number at the downstream part of the straight pass is shown in Fig. 11. The averaging area of 2–3D upstream of the turn was chosen so that the downstream turn effect can be excluded. In Fig. 11, the buoyancy parameter, $Gr_{\mathrm{m},q}/Re_{\mathrm{m}}^2$, is used as the horizontal axis. On the pressure surface, the buoyancy effect on Nu_{area} is large, and Nu_{area} of the aiding contribution cases (solid lines) are larger than those of the opposing contribution cases (broken lines). However, the detailed tendency differs depending on Re_* and Ro_* and the straightforward description on the buoyancy effect on Nu_{area} in the developed region cannot be made. The values on the suction surface show much smaller variation, and a slight increase is observed due to the buoyancy.

Fig. 12 shows the friction factor, f, normalized by using f_{B} in the following Blasius equation:

$$f_{\mathrm{B}} = 0.079 Re_{\mathrm{m}}^{-0.25}. \tag{17}$$

The precise values of f/f_{B} are shown in Table 1. In order to decompose the total pressure loss into the sharp-turn and straight-pass contributions, the following pressure loss coefficients, K_{turn} and K_{straight}, are also plotted in Fig. 12 [38]:

$$K_{\mathrm{turn}} = \frac{\Delta p_{\mathrm{turn}}}{\frac{1}{2}\rho U_{\mathrm{m}}^2} \quad \text{and} \quad K_{\mathrm{straight}} = \frac{\Delta p_{\mathrm{straight}}}{\frac{1}{2}\rho U_{\mathrm{m}}^2}. \tag{18}$$

Here, Δp_{turn} is the pressure loss associated with the sharp turn, and it is calculated by linearly extrapolating the area-averaged wall-pressure profile at the central region of the first and second straight passes in the direction toward the turn inlet and outlet locations at $z = 17$ for the turn A and at $z = 1$ for the turn B [38]. The straight pass component, $\Delta p_{\mathrm{straight}}$, was calculated from the linear pressure profile at the central region of the straight pass.

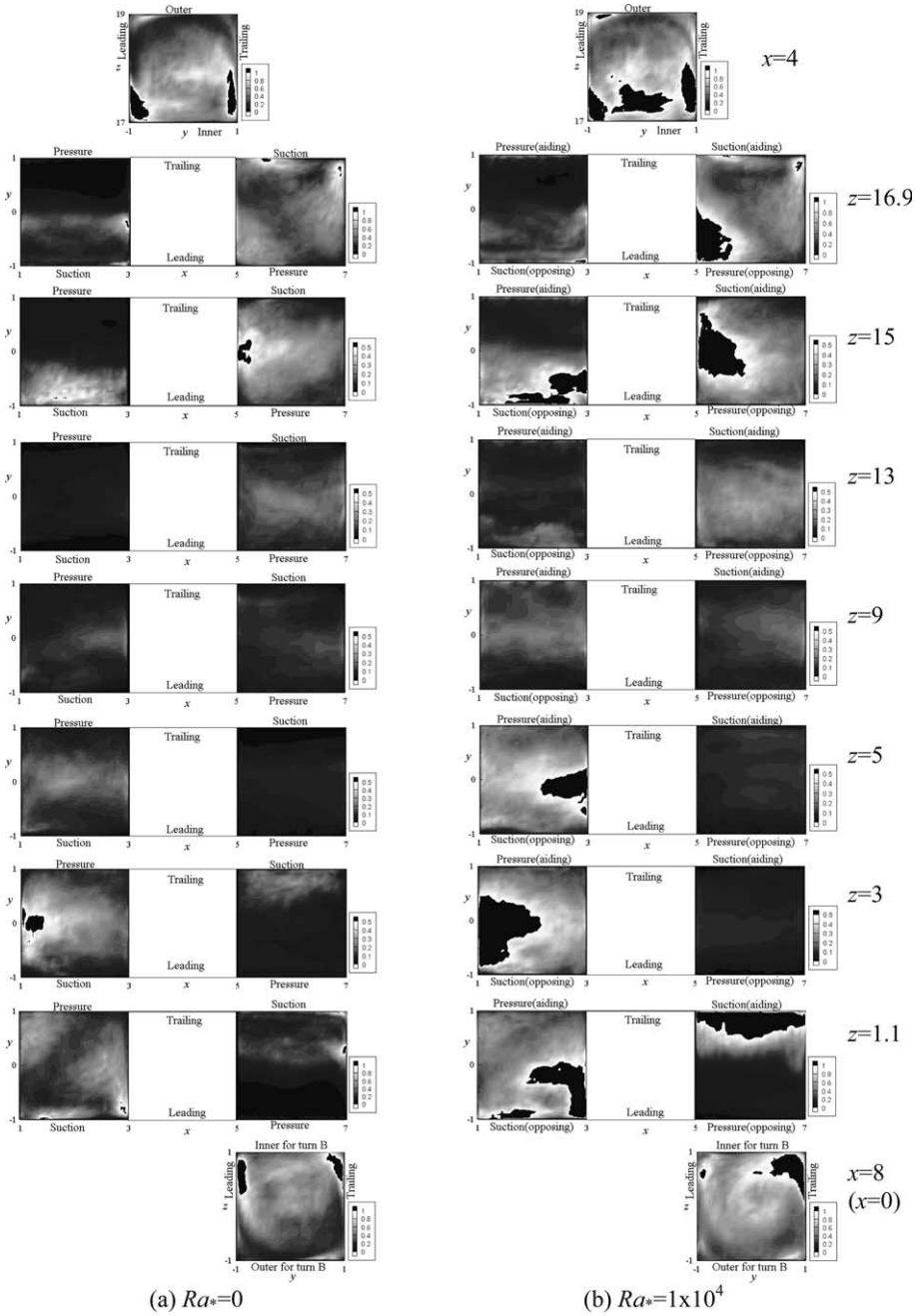

Fig. 8. Buoyancy effect on turbulent kinetic energy in planes normal to duct-axis for $Re_* = 1500$ and $Ro_* = 2$ (From top to bottom, $x = 4$, $z = 16.9$, 15, 13, 9, 5, 3, 1.1, and $x = 8$).

A small decrease of the f factor by the buoyancy force is observed in Fig. 12. This is contrary to the fact that the f factor gave a rapid increase by the introduction of the channel rotation (the rotation number effect) [26]. Without the buoyancy, K_{turn} is larger than K_{straight}. The buoyancy makes K_{turn} decrease both in the turns A and B with an exception for the turn B of $Re_* = 3500$, in which K_{turn} shows a slight increase. The value of K_{straight} in the second straight pass becomes negative, due to the positive pressure gradient in the streamwise direction which is caused by the coincidence of the main flow and buoyancy force directions: the main flow is driven by the buoyancy in the second straight pass (radially inward flow). The buoyancy increases and decreases K_{straight} in

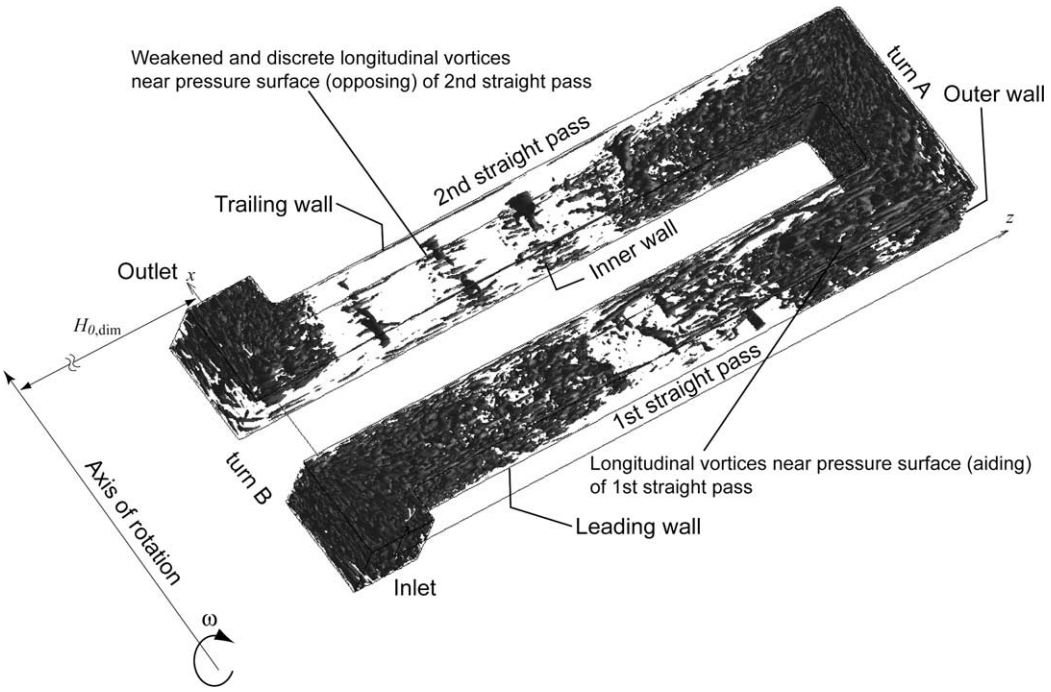

Fig. 9. Instantaneous vortex structure visualized as isosurface of $Q = 10$ ($Re_* = 1500$, $Ro_* = 2$, and $Ra_* = 1 \times 10^4$).

the first and second straight passes, respectively, and this opposing variation in K_{straight} cancels to each other. As a total, the pressure loss behavior of the channel is controlled by K_{turn}, and the f factor decreases as $Gr_{\mathrm{m},q}/Re_{\mathrm{m}}^2$ increases. As can be understood by the large variation of K_{turn} at $Gr_{\mathrm{m},q}/Re_{\mathrm{m}}^2 = 0$ for different Ro_*, K_{turn} is very sensitive to the rotation number, Ro_*. On the contrary, K_{straight} is insensitive to Ro_* at $Gr_{\mathrm{m},q}/Re_{\mathrm{m}}^2 = 0$.

Fig. 13 shows the Colburn's j factor normalized by using j_∞ calculated from Nu_∞ in Eq. (15). The precise values of j/j_∞ are shown in Table 1. In order to further examine the heat transfer efficiency taking the pressure loss into account, the heat transfer efficiency index, η_{eff}, was calculated by using the following equation [39]:

$$\eta_{\mathrm{eff}} = \frac{St/St_{\mathrm{smooth,stationary}}}{\left(f/f_{\mathrm{smooth,stationary}}\right)^{1/3}}. \tag{19}$$

As explained in [39], η_{eff} is the index of the heat conductance for equal pumping power and heat transfer surface area. As shown in Fig. 13, the j factor is insensitive to the buoyancy and stays almost constant. As a result, η_{eff} slightly increases with the increase of the buoyancy due to the decreased f factor seen in Fig. 12.

4. Conclusions

In order to investigate the centrifugal buoyancy effect on the heat transfer, the large eddy simulation of the two-pass square rotating channel with the 180-deg sharp turns was performed by varying the Rayleigh number. From the numerical results, the following conclusions were drawn.

Due to the aiding and opposing buoyancy contributions to the main flow, the velocity and temperature fields became different depending on the radial flow directions. The variation caused by the buoyancy was larger for the heat transfer on the pressure surface than that on the suction surface. When the instantaneous vortex structure was viewed, the longitudinal vortex structure was maintained near the pressure surface of the radially outward flow where the aiding buoyancy contribution worked, but that was weakened and became discrete near the pressure surface of the radially inward flow where the opposing buoyancy contribution worked.

The pressure loss coefficient of the sharp turn was decreased by the buoyancy, and that of the straight pass was increased and decreased in the first (radially outward flow) and second (radially inward flow) straight passes, respectively. Because the pressure losses of the two straight passes canceled to each other, the friction factor of the channel was controlled by the pressure loss of the sharp turn, and it decreased a little as the buoyancy increased. In the present buoyancy range, the Coburn's j factor stayed almost constant, and the heat transfer efficiency index was slightly increased by the buoyancy due to the decreased friction factor.

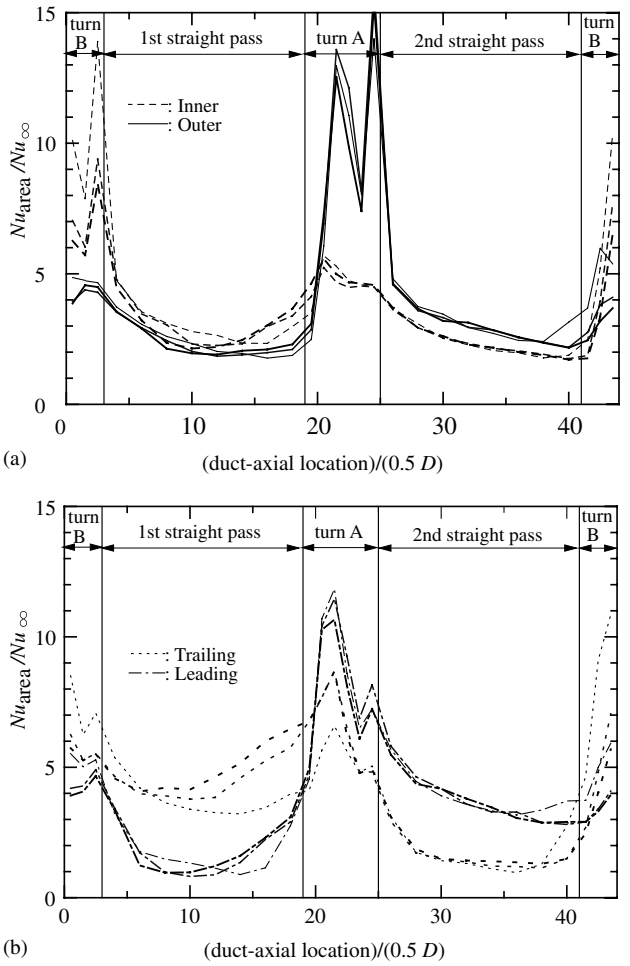

Fig. 10. Area-averaged Nusselt number variation in duct-axial direction for $Re_* = 1500$ and $Ro_* = 2$ (thin, middle, and thick lines are for $Ra_* = 0$, 5×10^3, and 1×10^4, respectively). (a) Inner and outer walls, (b) leading and trailing walls.

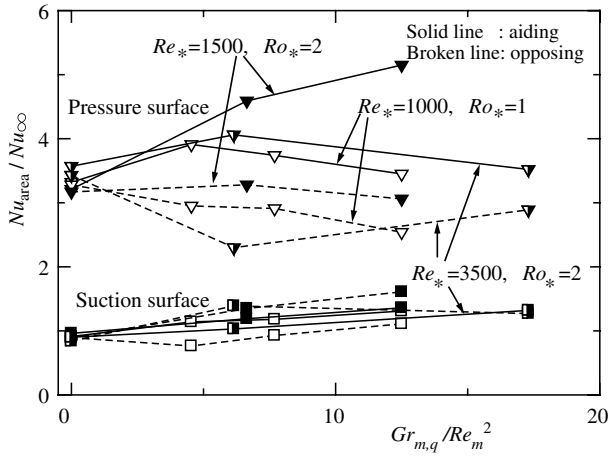

Fig. 11. Buoyancy effect on area-averaged Nusselt number at developed region in straight passes (averaging area was 2–3D upstream of turns. Open, filled, and half-filled symbols are for ($Re_* = 1000$, $Ro_* = 1$), ($Re_* = 1500$, $Ro_* = 2$), and ($Re_* = 3500$, $Ro_* = 2$), respectively. Symbols with solid and broken lines are for aiding and opposing buoyancy contributions, respectively).

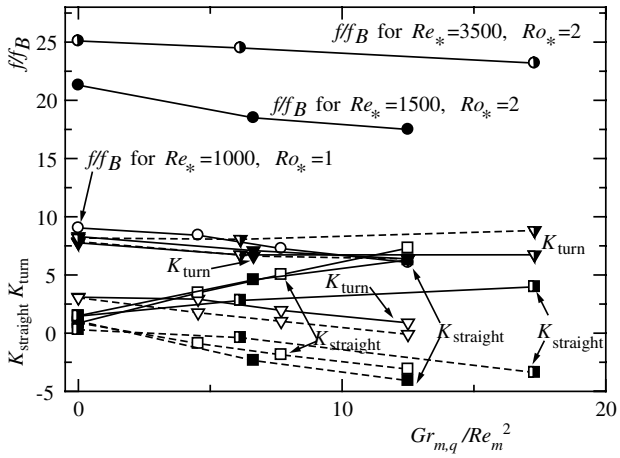

Fig. 12. Buoyancy effect on pressure loss (open, filled, and half-filled symbols are for ($Re_* = 1000$, $Ro_* = 1$), ($Re_* = 1500$, $Ro_* = 2$), and ($Re_* = 3500$, $Ro_* = 2$), respectively. Symbols with solid lines are for turn A or first straight pass, and those with broken lines are for turn B or second straight pass).

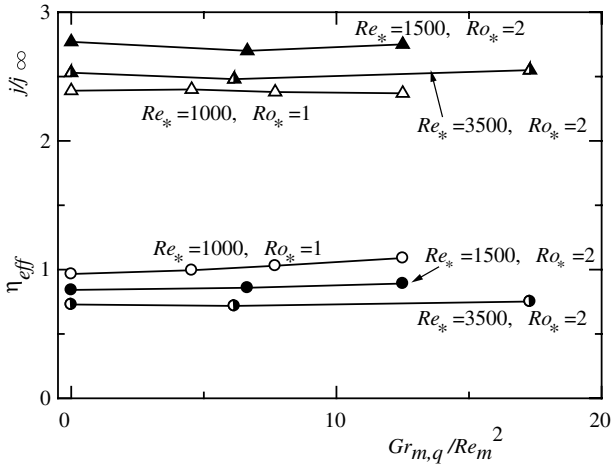

Fig. 13. Buoyancy effect on j factor and heat transfer efficiency index.

References

[1] J.-C. Han, Recent studies in turbine blade cooling, in: CD-ROM Proc. of the 9th Int. Symp. on Transport Phenomena and Dynamics of Rotating Machinery, Honolulu, Hawaii, US, Invited Lecture, 2002, 1–16.

[2] A. Murata, S. Mochizuki, M. Fukunaga, Detailed measurement of local heat transfer in a square-cross-section duct with a sharp 180-deg turn, Heat Transfer 1994, Proc. of Int. Heat Transf. Conf., Brighton, GB, vol. 4, 1994, pp. 291–296.

[3] S. Mochizuki, A. Murata, M. Fukunaga, Effects of rib arrangements on pressure drop and heat transfer in a rib-roughened channel with a sharp 180° turn, Trans. ASME, J. Turbomach. 119 (1997) 610–616.

[4] P.R. Chandra, J.C. Han, S.C. Lau, Effect of rib angle on local heat/mass transfer distribution in a two-pass rib-roughened channel, Trans. ASME, J. Turbomach. 110 (1988) 233–241.

[5] M. Hirota, H. Fujita, A. Syuhada, S. Araki, T. Yoshida, T. Tanaka, Heat/mass transfer characteristics in two-pass smooth channels with a sharp 180-deg turn, Int. J. Heat Mass Transfer 42 (1999) 3757–3770.

[6] S.V. Ekkad, J.C. Han, Detailed heat transfer distributions in two-pass square channels with rib turbulators, Int. J. Heat Mass Transfer 40-11 (1997) 2525–2537.

[7] T.M. Liou, C.C. Chen, T.W. Tsai, Liquid crystal measurements of heat transfer in a 180° sharp turning duct with different divider thicknesses, in: CD-ROM Proc. of the 8th

Int. Symp. on Flow Visualization, Sorrento, Italy, vol. 71, 1998, pp. 1–9.
[8] T. Astarita, G. Cardone, Thermofluidynamic analysis of the flow in a sharp 180° turn channel, Exp. Thermal Fluid Sci. 20 (2000) 188–200.
[9] S.Y. Son, K.D. Kihm, J.-C. Han, PIV flow measurements for heat transfer characterization in two-pass square channels with smooth and 90° ribbed walls, Int. J. Heat Mass Transfer 45 (2002) 4809–4822.
[10] J.-C. Han, Y.-M. Zhang, K. Kalkuehler, Uneven wall temperature effect on local heat transfer in a rotating two-pass square channel with smooth walls, Trans. ASME, J. Heat Transfer 115 (1993) 912–920.
[11] J.H. Wagner, B.V. Johnson, F.C. Kopper, Heat transfer in rotating serpentine passages with smooth walls, Trans. ASME, J. Turbomach. 113 (1991) 321–330.
[12] S. Mochizuki, S. Takamura, J. Yamawaki, S. Yang, W.-J. Heat, transfer in serpentine flow passages with rotation, Trans. ASME, J. Turbomach. 116 (1994) 133–140.
[13] J.A. Parsons, J.-C. Han, Y.-M. Zhang, Effect of model orientation and wall heating condition on local heat transfer in a rotating two-pass square channel with rib turbulators, Int. J. Heat Mass Transfer 38-7 (1995) 1151–1159.
[14] B.V. Johnson, J.H. Wagner, G.D. Steuber, F.C. Yeh, Heat transfer in rotating serpentine passages with trips skewed to the flow, Trans. ASME, J. Turbomach. 116 (1994) 113–123.
[15] S. Mochizuki, M. Beier, A. Murata, T. Okamura, Y. Hashidate, Detailed measurement of convective heat transfer in rotating two-pass rib-roughened coolant channels, ASME Paper, 96-TA-6, 1996.
[16] T.-M. Liou, C.-C. Chen, M.-Y. Chen, TLCT and LDV measurements of heat transfer and fluid flow in a rotating sharp turning duct, Int. J. Heat Mass Transfer 44 (2001) 1777–1787.
[17] B. Banhoff, U. Tomm, B.V. Johnson, I. Jennions, Heat transfer predictions for rotating U-shaped coolant channels with skewed ribs and with smooth walls, ASME Paper, 97-GT-162, 1997.
[18] Y.-L. Lin, T.I-P. Shih, M.A. Stephens, M.K. Chyu, A numerical study of flow and heat transfer in a smooth and ribbed U-duct with and without rotation, Trans. ASME, J. Heat Transfer 123 (2001) 219–232.
[19] A. Huser, S. Biringen, Direct numerical simulation of turbulent flow in a square duct, J. Fluid Mech. 257 (1993) 65–95.
[20] S. Gavrilakis, Numerical simulation of low Reynolds number turbulent flow through a straight square duct, J. Fluid Mech. 244 (1992) 101–129.
[21] R.K. Madabhushi, S.P. Vanka, Large eddy simulation of turbulence-driven secondary flow in a square duct, Phys. Fluids A 3-11 (1991) 2734–2745.
[22] A. Murata, S. Mochizuki, Effect of cross-sectional aspect ratio on turbulent heat transfer in an orthogonally rotating rectangular smooth duct, Int. J. Heat Mass Transfer 42 (1999) 3803–3814.
[23] J. Pallares, L. Davidson, Large eddy simulations of turbulent flow in a rotating square duct, Phys. Fluids 12-11 (2000) 2878–2894.
[24] A. Murata, S. Mochizuki, Large eddy simulation of turbulent heat transfer in an orthogonally rotating square duct with angled rib turbulators, Trans. ASME J. Heat Transfer 123 (2001) 858–867.
[25] A. Murata, S. Mochizuki, Effect of centrifugal buoyancy on turbulent heat transfer in an orthogonally rotating square duct with transverse or angled rib turbulators, Int. J. Heat Mass Transfer 44 (2001) 2739–2750.
[26] A. Murata, S. Mochizuki, Large eddy simulation of turbulent heat transfer in a rotating two-pass smooth square channel with sharp 180-deg turns, Int. J. Heat Mass Transfer 47 (2004) 683–698.
[27] A. Murata, S. Mochizuki, Effect of rib orientation and channel rotation on turbulent heat transfer in a two-pass square channel with sharp 180-deg turns investigated by using large eddy simulation, Int. J. Heat Mass Transfer 47 (2004) 2599–2618.
[28] S.V. Patankar, C.H. Liu, E.M. Sparrow, Fully developed flow and heat transfer in ducts having streamwise-periodic variations of cross-sectional area, Trans. ASME, J. Heat Transfer 99 (1977) 180–186.
[29] T. Kajishima, T. Ohta, K. Okazaki, Y. Miyake, High-order finite-difference method for incompressible flows using collocated grid system, JSME Int. J., Series B 41-4 (1998) 830–839.
[30] C. Meneveau, T.S. Lund, W.H. Cabot, A Lagrangian dynamic subgrid-scale model of turbulence, J. Fluid Mech. 319 (1996) 353–385.
[31] P. Moin, K. Squires, W. Cabot, S. Lee, A dynamic subgrid-scale model for compressible turbulence and scalar transport, Phys. Fluids A 3-11 (1991) 2746–2757.
[32] F.H. Harlow, J.E. Welch, Numerical calculation of time-dependent viscous incompressible flow of fluid with free surface, Phys. Fluids 8-12 (1965) 2182–2189.
[33] J. Kim, P. Moin, Application of a fractional-step method to incompressible Navier–Stokes equations, J. Comp. Phys. 59 (1985) 308–323.
[34] Y. Zang, R.L. Street, J.R. Koseff, A non-staggered grid, fractional step method for time-dependent incompressible Navier–Stokes equations in curvilinear coordinates, J. Comp. Phys. 114 (1994) 18–33.
[35] W.M. Kays, M.E. Crawford, Convective Heat and Mass Transfer, third ed., McGraw-Hill Inc, New York, 1993, p. 316.
[36] G.K. Batchelor, An Introduction to Fluid Dynamics, Cambridge University Press, 1967, pp. 555–559.
[37] J.C.R. Hunt, A.A. Wray, P. Moin, Eddies, stream, and convergence zones in turbulent flows, Center for Turbulence Research Report, CTR-S88, 1988.
[38] D.E. Metzger, C.W. Plevich, C.S. Fan, Pressure loss through sharp 180deg turns in smooth rectangular channels, J. Eng. Gas Turbines Power 106 (1984) 677–681.
[39] D.L. Gee, R.L. Webb, Forced convection heat transfer in helically rib-roughened tubes, Int. J. Heat Mass Transfer 23 (1980) 1127–1136.